Research on Engineering Structures & Materials
www.jresm.org

Research Article

Flexural behavior and ultimate capacity formulation of prestressed Steel-UHPC composite beams

Jingmin Wang [*,a]

School of Architecture Engineering, Yangzhou Polytechnic Institute, Yangzhou, China

Article Info

Article History:

Received 28 Aug 2026
Accepted 08 Oct 2026

Keywords:

Prestressed steel-UHPC beams;
Flexural behavior;
Strain compatibility;
Ultimate moment capacity;
Parameter sensitivity

Abstract

How prestressing strands and embedded steel sections jointly govern cracking, flexural resistance and deformation capacity in UHPC beams remains insufficiently quantified. Existing studies mainly address individual strengthening mechanisms, leaving the interaction between prestressing degree and steel-section ratio, and their relative importance among design parameters, insufficiently resolved. Five full-scale beams were tested under monotonic four-point loading, and an OpenSees model was used to compare 24 cases across eight design parameters. A section-equilibrium formulation accounts for UHPC compression and fiber tension, the embedded steel profile, longitudinal reinforcement and prestressing strands. The calculated-to-test moment ratio has a mean of 1.008 and a sample standard deviation of 0.031. Relative to the non-prestressed beam, the L2 cracking load increases by 68.3%. Increasing strand diameter from 12.7 to 17.8 mm increases peak load by 16.72%, while increasing steel yield strength from 235 to 460 MPa increases peak load by 31.38%. The sensitivity matrix distinguishes the dominant parameter for cracking resistance from that for peak-load response, and the ductility comparison identifies how the effect of prestress changes with steel-section ratio. These comparisons quantify the combined strengthening mechanism and connect parameter selection to crack control, flexural capacity and deformation demand.

© 2026 MIM Research Group. All rights reserved.

1. Introduction

Prestressed steel Ultra-High-Performance Concrete (UHPC) beams are composite components that combine prestressing technology with embedded steel bars. They embed steel bars within the UHPC section and tension prestressed steel strands, thereby forming a flexural composite structure. Moment-curvature analysis has been used to evaluate the flexural strength of prestressed UHPC beams; the resulting design approach includes crack localization and section-size effects [1]. The force process of prestressed steel UHPC beams involves the multiple couplings of UHPC's nonlinear constitutive behavior, bond-sliding, and prestress effects. The mechanical behavior of these components is more complex than that of traditional ones, and their core material, UHPC, has extremely high Compressive Strength (CS), tensile toughness, and good durability properties. Four-point bending tests have examined steel plate-UHPC strengthening of RC beams, and analytical formulations incorporating UHPC strain hardening predict cracking and ultimate resistance [2]. Tests in the negative-moment region have compared steel-UHPC and steel-ordinary concrete composite beams, showing improvements in cracking load and flexural ductility when UHPC is used [3].

As structural engineering moves towards lightweight and high durability, traditional reinforced concrete components have difficulty meeting the increasing requirements for Bearing Capacity

*Corresponding author: jingmin_wang@outlook.com
[a]orcid.org/0009-0004-6601-025X
DOI: http://dx.doi.org/10.17515/resm2026-2268vk0828rs

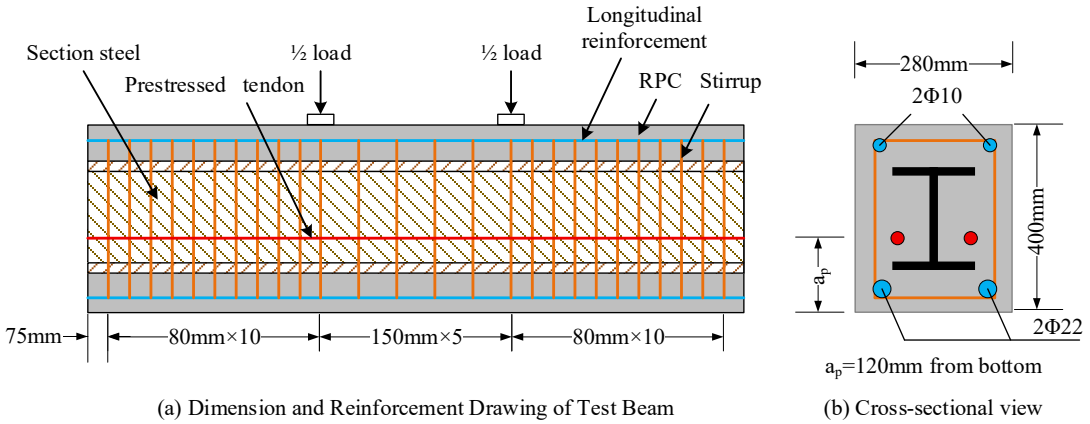
(BC) and deformation control [4]. Prestressed concrete can improve crack resistance and stiffness, but it has limited improvement in section ductility and is prone to brittle failure under high stress [5]. Steel-concrete composite materials have good ductility and BC, but their crack resistance is insufficient, and cracks occur at lower loads, making them unable to meet the requirements of high durability environments [6-7]. Combining the three can achieve complementary advantages and become an important development direction for high-performance composite structures. Currently, research on the synergistic enhancement of the Flexural Performance (FP) of such components by prestress and steel bars continues to be weak, without adequate systematic understanding of the synergistic influence laws of prestress intensity and steel bar ratio [8]. Most related studies focus on material constitutive relationships or the performance of single enhancement methods for component properties, and there is a lack of in-depth exploration of the quantitative impact of various design parameters on BC and deformation performance in the dual-enhancement system. Finite element parameter analysis has not yet formed a systematic sensitivity evaluation framework [9-10].

However, literature on the synergistic action of prestressed UHPC beams and embedded steel profiles within a dual-enhancement system remains limited. In particular, the interaction between prestressing degree and steel-section ratio has not been sufficiently connected to cracking, ductility and the relative influence of design parameters. Mechanically, plane-section compatibility links UHPC strain to the strains of the embedded steel profile, longitudinal bars and prestressing strands. Axial equilibrium between UHPC compression, fiber-bridging tension and the steel resultants determines the neutral-axis depth; their lever arms determine flexural resistance, including the strand stress increment caused by bending. Combining five-beam tests with section equilibrium and an eight-parameter sensitivity matrix provides a common basis for quantifying this interaction and distinguishing crack-control parameters from capacity-governing parameters.

2. Experimental Materials and Methods

2.1 Specimen Design and Fabrication

To explore the combined influence of prestressing force and steel reinforcement ratio on the flexural behavior of prestressed steel UHPC beams, a total of 5 full-scale test beams are designed and fabricated in the experiment. Among them, 4 are prestressed steel UHPC beams (labeled as L1 to L4), and their dimensions and reinforcement details are exhibited in Figure 1.



(a) Dimension and Reinforcement Drawing of Test Beam (b) Cross-sectional view

Fig. 1. Dimensions and reinforcement of the test beam

In Figure 1, the Cross-Sectional (CS) dimensions of all specimens are designed as 280mm × 400mm, and the total length of the beams is 2500mm, with the calculation span being 2250mm. Another beam is a steel UHPC control beam without prestressing (numbered L0). The embedded Steel Sections (SSs) are all welded with Q345 grade Steel Plates (SP), and the matrix material is UHPC, the longitudinal reinforcement is HRB500, and the stirrups are HRB400 steel. The measured yield strength of the longitudinal reinforcement is 537.8 MPa. Four-point bending tests on prestressed I-beams with UHPC layers characterize their flexural response, and changes in layer length affect resistance and failure mode [11]. By changing the CS dimensions of the embedded SSs (240mm ×

120mm × 6mm × 8mm and 240mm × 150mm × 8mm × 10mm, i.e., CS height × flange width × web thickness × flange thickness) and the nominal diameter of the prestressing strands, cross-parameter comparisons are achieved [12-13]. The specific CS geometric dimensions, steel configuration, and parameter combinations of the test beams are exhibited in Table 1.

Table 1. Main design parameters and mechanical properties of materials for the test beam

Specimen No.	Section Size (mm)	SS dimensions h × b × t_w × t_f (mm)	Prestressing tendon	Steel Ratio ρa (%)	λ	f_{cu} (MPa)	f_t (MPa)	f_{ya} (MPa)	f_{yr} (MPa)	f_{pt} (MPa)
L0	280×400	240×120×6×8	/	2.91	0.00	147.3	11.6	367.4	537.8	/
L1	280×400	240×120×6×8	2 × 12.7 mm	2.91	0.19	149.1	12.1	367.4	537.8	2028.4
L2	280×400	240×120×6×8	2 × 15.2 mm	2.91	0.26	146.8	11.4	367.4	537.8	2074.1
L3	280×400	240×150×8×10	2 × 12.7 mm	4.25	0.15	148.6	11.9	367.4	537.8	2028.4
L4	280×400	240×150×8×10	2 × 15.2 mm	4.25	0.21	150.2	12.3	367.4	537.8	2074.1

Note: fcu represents the measured CS of UHPC cubes. ft represents the measured axial tensile capacity of UHPC. fya represents the measured Yield Strength (YS) of SSs. fyr represents the measured YS of HRB500 Longitudinal Reinforcement (LR). fpt represents the measured ultimate tensile strength of prestressed steel strands.

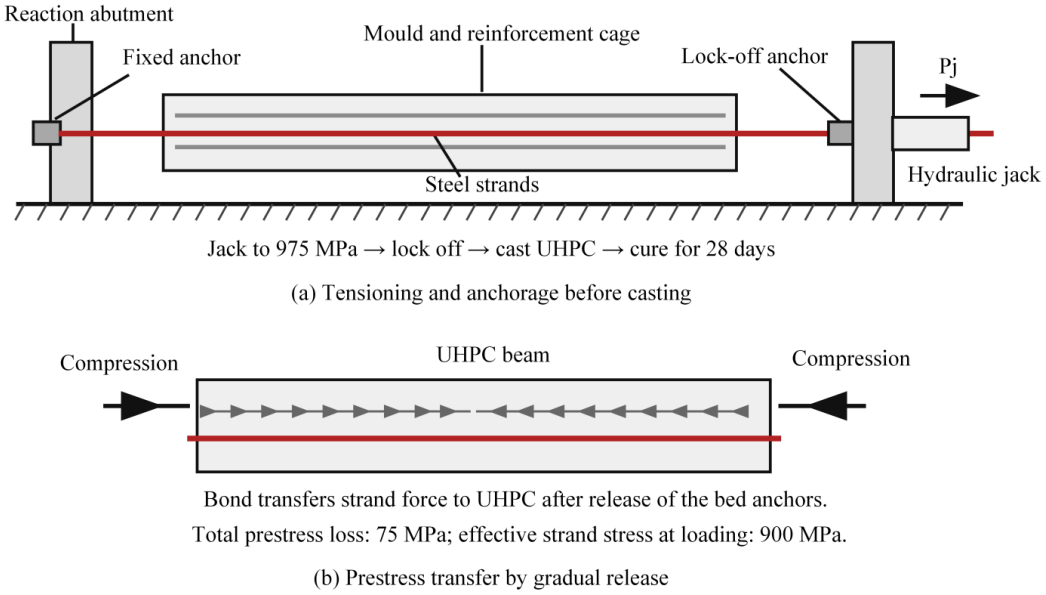


Fig. 2. Strand tensioning and prestress transfer mechanism

The longitudinal reinforcement comprises two 10 mm top bars and two 22 mm bottom bars, with layer centroids 40 and 360 mm below the top surface. Closed 8 mm stirrups are spaced at 80 mm in the shear spans and 150 mm in the middle zone. The seven-wire strands have nominal diameters of 12.7 and 15.2 mm and total areas of 197.4 and 280.0 mm2, respectively. The strand centroid is 120 mm above the bottom surface. Increasing ap therefore moves the strands upward and reduces their flexural lever arm. The steel-section ratio and prestressing degree are $\rho_a = A_a/(bh)$ and $\lambda = A_p f_{pt}/(A_p f_{pt} + A_a f_{ya} + A_s f_{yr})$. Here, A_a, A_s and A_p denote the steel-profile area, total longitudinal-bar area and total strand area; b and h are section width and depth. The I-section notation is height × flange width × web thickness × flange thickness.

The beams were pretensioned on a rigid bed using wedge anchors at the abutments. The strands were jacked to 975 MPa and held during casting and curing; prestress was transferred gradually after 28 days. Anchorage seating, elastic shortening and time-dependent losses totaled 75 MPa at loading, giving an effective stress of 900 MPa. The external bed anchors were released after transfer, and prestress was retained by the bonded strands. The tensioning and transfer mechanism is shown in Figure 2. In Figure 2(a), the rigid-bed abutments resist the jacking force

while the strands remain anchored during casting and curing. In Figure 2(b), gradual release transfers strand force to the hardened UHPC through bond, establishing compression in the beam.

2.2 Material Constitutive Relationship

The UHPC used in the test did not contain coarse aggregates and is internally reinforced with copper-plated micro-fiber steel fibers with a volume content of 2.5%. After being cured under standard conditions for 28 days, the measured mean CS fcu of the cubic specimens is 148.4 MPa, and the axial tensile capacity ft is 11.9 MPa. Since UHPC can still provide certain residual tensile strength by relying on the bridging effect of the steel fibers after being cracked under tension, when conducting the analysis of the entire loading process and subsequent finite element simulations, its tensile contribution must be considered. Therefore, the compressive constitutive model of UHPC adopts a segmented model with ascending and descending branches, and the tensile constitutive model adopts a piecewise-linear model including initial cracking, hardening and post-peak softening. For built-in steel bars and ordinary reinforcing bars, an ideal Elastic-Plastic (EP) double-spline model is used. For prestressed steel cables, a triple-spline model is adopted to reflect their proportional limit, yield limit and ultimate tensile strength [14-16]. The UHPC mixture and fiber properties are listed in Table 2. The water-to-binder ratio is 0.18, with cement and silica fume forming the binder. The fiber aspect ratio is 65.

Table 2. UHPC mixture proportions and steel-fiber properties

Constituent / property	Value
Cement / silica fume	800 / 200 kg/m^3
Quartz powder / quartz sand	150 / 1000 kg/m^3
Mixing water / superplasticizer	180 / 20 kg/m^3
Steel fiber volume fraction	2.5%
Fiber length / diameter	13 / 0.20 mm
Fiber tensile strength	2850 MPa

2.3 Loading Scheme and Measurement Point Layout

The FP test is conducted on the 2000kN microcomputer-controlled electro-hydraulic servo universal testing machine system in the structural engineering laboratory. Before the formal loading, a 50kN pre-load is applied to eliminate the contact gap between the support and the specimen and to make sure the reliability of the data acquisition system. During the formal loading, the force control mode is adopted before the expected yield of the test beam, with each load increment of 50kN, and the data is recorded after holding the load for 3 minutes. When the deflection at the Mid-Span (MS) grows sharply and a significant inflection point appeared in the load-deflection curve, it is determined that the specimen has entered the yield state, and then the displacement control mode is switched, with a loading rate of 1.0mm/min, until the BC drops to 85% of the peak load or the specimen suffered severe damage, and the test is stopped. The schematic diagram of the loading device and the location of the measuring points is exhibited in Figure 3.

In Figure 3, the entire length of the test beam is 2500mm. Both ends of the beam are supported 125mm away from the beam ends. Thus, the calculated span is determined to be 2250mm. The loading method is symmetrical two-point monotonic static loading. By distributing the beam, a pure Bending Section (BS) of 700mm length is formed at the MS, and the lengths of the bending-shear sections on both sides are both 775mm. To comprehensively capture the data of the entire force application process, resistance strain gauges are arranged at the MS section and the upper and lower flanges, the center of the web, and the surface of the LR of the SP. Five electronic displacement meters with a measurement range of 100 mm and an accuracy of ±0.1 mm are distributed at the supports, the loading points, and the MS section to monitor the MS deflection and the settlement of the supports.

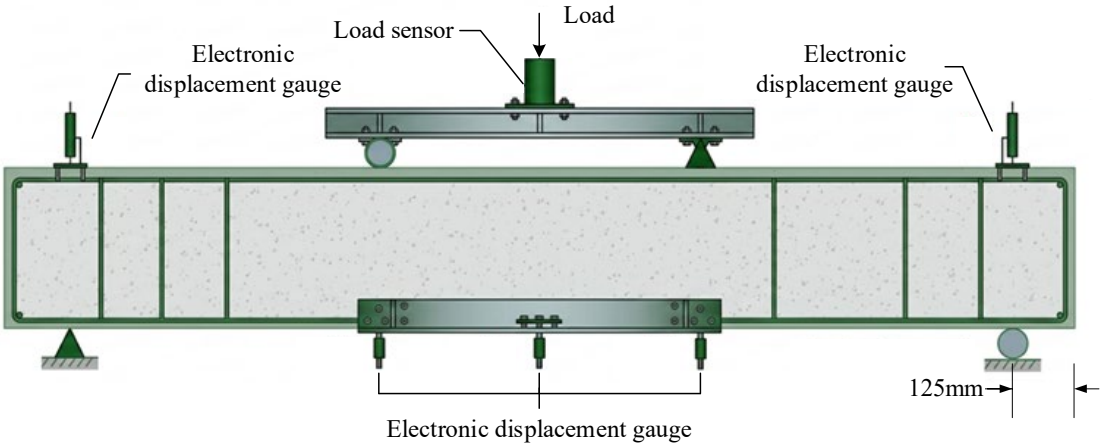


Fig. 3. Schematic diagram of the test loading device and measurement point arrangement

2.4 Establishment of FEM

A nonlinear FEM of prestressed steel UHPC beams was developed in OpenSees to further explore the effects of more parameters on flexural performance [17]. UHPC is represented by eight-node SSPbrick elements, the steel profile by four-node ShellMITC4 elements, and reinforcing bars and strands by two-node truss elements. Translational compatibility ties the embedded steel nodes to the surrounding concrete. Experiments on continuous beams have quantified the flexure-induced stress increase of unbonded tendons [18]. To accurately reflect the stiffness degradation and damage accumulation of UHPC during the loading process, the concrete material adopts the OpenSees nDMaterial ASDConcrete3D plastic-damage model. The tensile and compressive backbones are supplied as total-strain–stress pairs through -Te/-Ts and -Ce/-Cs, with separate damage histories through -Td/-Cd. Tensile bridging and compressive softening are included in the UHPC envelopes [19].

Full bond is adopted because the encased steel and bonded strands transfer force through the surrounding UHPC, and the section strain profiles retain approximate compatibility up to the peak load. This idealization targets global flexural resistance; local bond-slip can reduce post cracking stiffness and increase deflection, and full bond can overestimate resistance when interface slip is appreciable. Prestress is imposed as an initial-strain offset equivalent to cooling: $\Delta T = -\sigma_{pe}/(E_p\alpha)$ and $\varepsilon_0 = -\alpha\Delta T = \sigma_{pe}/E_p$. With $E_p = 195000$ MPa, $\alpha = 1.2 \times 10^{-5}$ per °C and $\sigma_{pe} = 900$ MPa, the equivalent temperature change is −384.62 °C and the tensile material offset is 0.004615. InitStrainMaterial wraps the strand law, and an initial equilibrium step establishes the prestressed state before external loading.

Using positive strain and stress magnitudes, the tensile knots are $(\varepsilon_{ti}, f_{ti}) = \{(0,0), (f_{cr}/E_c, f_{cr}), (\varepsilon_{tp}, f_t), (\varepsilon_{tu}, 0)\}$. The compressive knots are $(\varepsilon_{ci}, f_{ci}) = \{(0,0), (f_{c1}/E_c, f_{c1}), (\varepsilon_{cp}, f_c), (\varepsilon_{cu}, f_{c,res})\}$. The tensile and compressive branches are defined by consecutive knots in the form given by Equation. (1).

$$\begin{cases} \sigma_t(e) = f_{ti} + (f_{t,i+1} - f_{ti})(e - \varepsilon_{ti})/(\varepsilon_{t,i+1} - \varepsilon_{ti}), & \varepsilon_{ti} \le e \le \varepsilon_{t,i+1}. \\ \sigma_c(e) = f_{ci} + (f_{c,i+1} - f_{ci})(e - \varepsilon_{ci})/(\varepsilon_{c,i+1} - \varepsilon_{ci}), & \varepsilon_{ci} \le e \le \varepsilon_{c,i+1}. \end{cases} \quad (1)$$

In Equation (1), E_c is the initial elastic modulus; f_{cr} and f_t are the first-cracking and peak tensile stresses; ε_{tp} and ε_{tu} are the tensile peak and terminal strains. In compression, f_{c1} marks the end of the initial elastic branch, f_c is the peak stress at ε_{cp}, and $f_{c,res}$ is the residual stress at ε_{cu}. The intervals before and after each peak represent hardening and softening, respectively. Total strains are entered directly into the material command.

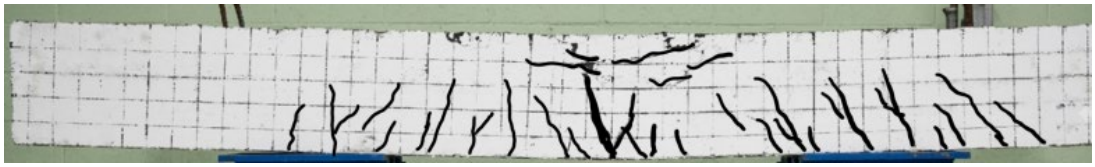
The adopted parameters are $E_c = 50000$ MPa, $f_c = 0.85f_{cu}$, $f_{c1} = 0.4f_c$, $\varepsilon_{cp} = 0.0035$, $\varepsilon_{cu} = 0.008$ and $f_{c,res} = 0.2f_c$; in tension, $f_{cr} = 0.8f_t$, $\varepsilon_{tp} = 0.0008$ and $\varepsilon_{tu} = 0.020$. Steel sections and longitudinal bars

use $E_s = 200000$ MPa with the yield strengths in Table 1. The strand law linearly connects $(0,0)$, $(0.8f_{pt}/E_p, 0.8f_{pt})$, $(0.010, 0.9f_{pt})$ and $(0.035, f_{pt})$.

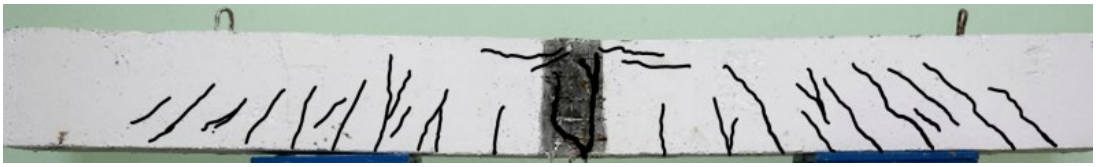
3. Experimental Outcomes and Analysis

3.1 The Entire Bending Process and Failure Mode of The Test Beam

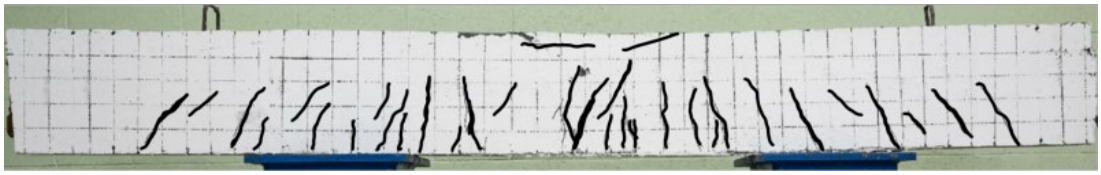
In the initial loading regime, the specimen's stiffness was relatively high, and the MS deflection was basically in a linear relationship with the applied load. No Crack Development (CD) was observed during this stage. When the load reached the cracking critical value, the bottom of the pure BS of the UHPC reached the tensile limit, and the first vertical crack appeared at the MS. The crack distribution pattern and final failure characteristics of the typical specimen are exhibited in Figure 4. In Figure 4, the prestressed state had an impact on the advancement trajectory of cracks. For the non-prestressed beam L0, after cracking, the number of cracks in the pure BS was relatively small. As the load increased, a main crack with a rapidly increasing width gradually formed at the MS and rapidly extended to the Compression Zone (CZ), showing a localized failure trend. However, for the prestressed beam L4, under the action of pre-stress, the formation of the first cracks was delayed. During the loading process, new vertical cracks continuously emerged in the pure BS, and the overall crack morphology was characterized by small spacing, uniform distribution, and fine width. When the load further increased, the tensile reinforcement and the lower flange of the SS successively yielded, and the section stiffness began to deteriorate, causing the specimen to enter the EP stage.



(a) Front Crack Distribution Diagram of L0



(b) Distribution Diagram of Cracks on the Reverse Side of L0



(c) Distribution Diagram of Front Cracks of L4



(d) Distribution Diagram of Cracks on the Reverse Side of L4

Fig. 4. Typical crack distribution and failure morphology of the test beam

After that, new cracks in the pure BS basically did not emerge, and the loading deformation mainly transformed into the widening and upward extension of existing cracks. When reaching the peak load, the Neutral Axis (NA) moved upward, and the CZ edge of the UHPC in the pure BS reached the ultimate compressive strain and underwent local crushing. In general, all the test beams exhibited the appropriate reinforcement failure characteristics of the tensile steel yielding first and the CZ concrete crushing later. However, the application of prestress dispersed the crack stress, avoided

the concentrated expansion of the main crack, and improved crack control before failure; the deflection ductility is assessed separately from the measured yield and peak points. The load-span deflection curves of each specimen during the entire loading process are exhibited in Figure 5.

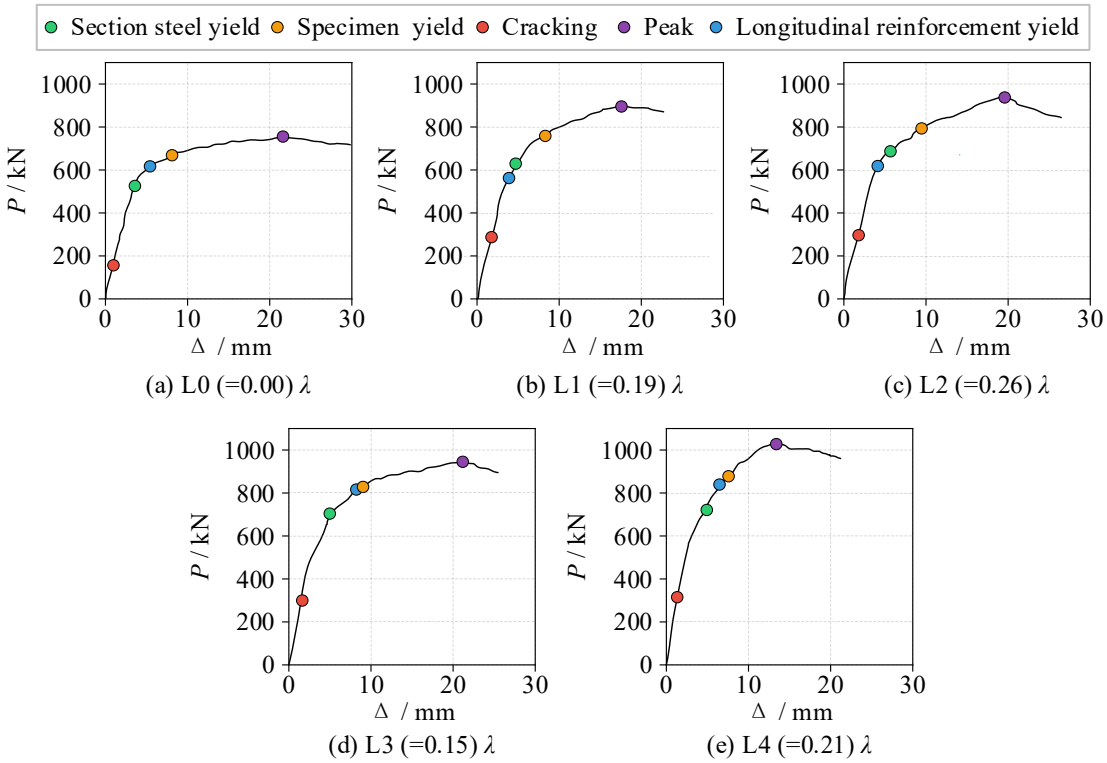


Fig. 5. Load–MS deflection curve

In Figure 5, the behavior of the specimen could be attributed to three stages: the elastic working period, the EP development period, and the plastic failure period. Firstly, in the elastic stage, since UHPC and the steel bars had excellent tensile properties, after the specimen cracked, although the slope of the curve decreased, there was no obvious mutation point, implying that the specimen still maintained a certain overall stiffness. Entering the EP stage, as the bottom flange and the lower LR of the steel bar yielded, the stiffness of the specimen significantly decreased. Meanwhile, the MS deflection increased, and the increase in BC was limited. Entering the plastic stage, the load did not show a significant change, and the MS deformation increased sharply. After the specimen reached the peak load, the curve flattened and descended slowly, implying that the specimen had good ductility. The comparison of the characteristic loads and MS deflection measured outcomes of each test beam is exhibited in Table 3.

Table 3. Characteristic loads and deflection ductility of the test beams

Beam	λ	Pcr	Pya	Pys	Py	Pm	Gain (%)	μ
L0	0.00	182.50	525.14	615.32	668.75	769.45	/	2.66
L1	0.19	283.60	625.42	586.18	765.84	898.23	16.74	2.12
L2	0.26	307.12	675.34	616.24	798.65	952.88	23.84	2.07
L3	0.15	295.65	694.55	824.61	832.12	950.24	23.50	2.36
L4	0.21	326.12	738.45	843.42	877.39	1042.61	35.50	1.76

Note: Loads are in kN and deflections in mm. $\mu = \Delta_u/\Delta_y$, where Δ_y corresponds to the specimen yield load P_y and Δ_u to the peak load P_m. Peak-load gains are relative to L0. P_{cr}, P_{ya} and P_{ys} denote cracking, steel-profile yielding and longitudinal-bar yielding.

From Table 3, prestressing increases the cracking loads of L1 and L2 by 55.4% and 68.3% relative to L0, while their peak loads increase by 16.74% and 23.84%. Increasing the steel-section ratio from 2.91% to 4.25% raises the L4 peak load by 9.42% relative to L2. The ductility indices are 2.66, 2.12, 2.07, 2.36 and 1.76 for L0–L4. Prestressing therefore does not uniformly increase deflection

ductility. Increasing the steel-section ratio increases ductility from L1 to L3 but decreases it from L2 to L4, showing the interaction with strand area.

3.2 Analysis of Section SD and Crack Characteristics

To make sure whether the prestressed steel UHPC beam conformed to the assumption of a flat section during the bending process, strain gauges were evenly spaced along the height of the MS surface of the specimen. Meanwhile, strain measurement points were also set up at the LR, the upper and lower flanges of the SS, and the web of the beam. The strain data of the MS section of 5 specimens under each load level were extracted, and the Strain Distribution (SD) curves along the section height were plotted, as exhibited in Figure 6.

In Figure 6, under the action of various loads, the CS strains of the 5 specimens distributed along the height were all in a straight line as a whole, implying that the prestressed steel UHPC beam basically followed the assumption of a flat section throughout the loading process. At the heights where the steel bars and longitudinal bars were located, the strain data points slightly deviated from the fitted straight line, which was caused by the slight adhesion slip between the steel and the surrounding UHPC. Based on the measured data from the experiments and the theoretical outcomes, the NA positions and CD characteristics of each specimen were analyzed. The NA positions and CD characteristics are exhibited in Figure 7.

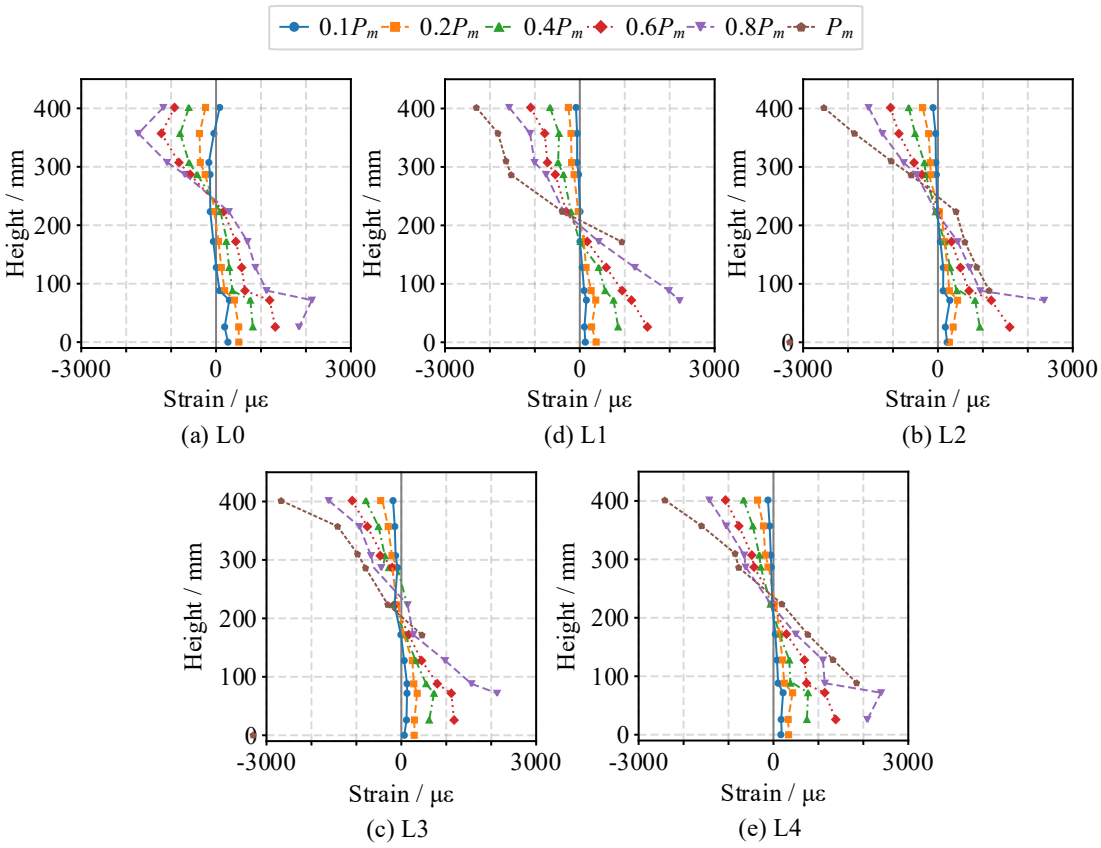
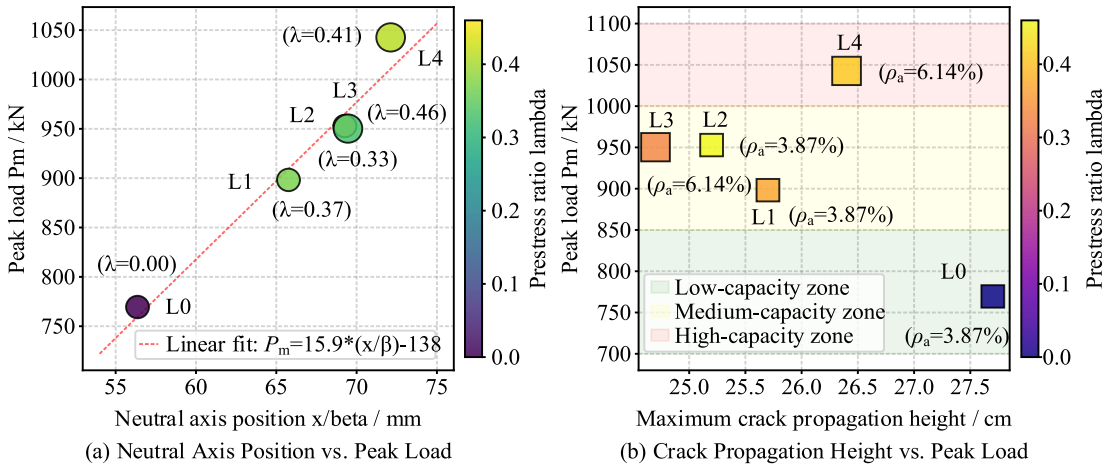


Fig. 6. Evolution of height-SD across the cross-section. The strain is expressed in micro-strain (με)

In Figure 7(a), the NA positions of the 5 specimens were all located near the upper flange of the SS (within the range of 56.36 to 72.12 mm). With the increase in the pre-stress force, the NA position showed a downward trend: the NA of L0 (λ = 0) was the highest (56.36 mm), while that of L4 (λ = 0.21) was the lowest (72.12 mm), with a downward shift of 15.76 mm. This phenomenon indicated that the introduction of pre-stress caused a change in the initial stress distribution of the section, and the height of the CZ increased accordingly. From the relationship between the peak load and the NA position, there was a certain positive correlation between them, that is, the lower the NA position (the larger the height of the CZ), the higher the peak load. This was consistent with the mechanical mechanism by which UHPC exhibited its CS to its full potential. The NA positions of L3

and L4 were close (69.46 mm and 72.12 mm), but the peak load of L4 (1042.61 kN) was higher than that of L3 (950.24 kN), implying that the contribution of the steel reinforcement rate to the BC was not only achieved by changing the NA position, but also through the tensile resistance of the SS itself.

Figure 7(b) exhibits that the max extension height of cracks at the peak load of each specimen is concentrated within the range of 24.7 to 27.7 cm, approximately 62% to 69% of the beam height (400 mm). The max extension height of the crack at L0 was the largest (27.7 cm), while the crack heights of the prestressed specimens L1 to L4 decreased (24.7 to 26.4 cm), implying that the prestress inhibited the upward expansion of cracks. From the trend of the scatter plot distribution, there was no obvious linear relationship between the max extension height of the crack and the peak load. However, the crack heights of the prestressed specimens were generally lower than those of the non-prestressed specimens, reflecting the control effect of prestress on the development of cracks. Although L4 had the highest peak load (1042.61 kN), its max extension height of the crack (26.4 cm) was still lower than that of L0 (27.7 cm), implying that the synergistic effect of high steel ratio and prestress advanced the BC while also controlling the development of cracks. In summary, prestress improved the overall mechanical performance of the section by increasing the height of the CZ and inhibiting the expansion of cracks.



(a) Neutral Axis Position vs. Peak Load (b) Crack Propagation Height vs. Peak Load

Fig. 7. Position of the NA and height of crack propagation

3.3 Ultimate Moment Formulation

The plane-section response in Figure 6 permits a strain-compatible calculation. Let y be measured downward from the top surface and c denote neutral-axis depth. At the compression-controlled ultimate state, the extreme compressive strain is 0.0035. The net UHPC area excludes the embedded profile, longitudinal bars and strands. The section strain and reinforcing-steel constitutive laws are given in Equation (2).

$$\varepsilon(y) = \varepsilon_{cu}^{*}(y/c - 1), \quad \varepsilon_{cu}^{*} = 0.0035; \quad \sigma_j(y) = max[-f_{yj}, min(E_s\varepsilon(y), f_{yj})], j = a, s. \tag{2}$$

UHPC stresses follow the tensile and compressive envelopes in Section 2.4. Separate integrations over the upper flange, web and lower flange retain the elastic or yielded stress distribution in each part. The strand stress follows its trilinear law, with the prestress strain included, as shown in Equation (3).

$$\varepsilon_p = \sigma_{pe}/E_p + \varepsilon(y_p) - \varepsilon_{ce,p}, \quad f_{ps} = F_p(\varepsilon_p), \quad \varepsilon_{ce,p} = -[P_p/(bh) + P_p e_p^2/I_g]/E_c. \tag{3}$$

In Equation (3), $y_p = h - a_p$, $e_p = y_p - h/2$, $P_p = A_p\sigma_{pe}$ and $I_g = bh^3/12$. The initial concrete strain at the strand level is $\varepsilon_{ce,p}$. The signed forces and their first moments about the neutral axis are defined as shown in Equation (4).

$$\begin{cases} N_{cc} = \int_{A_{c,c}} \sigma_c \, dA, \quad N_{ct} = \int_{A_{c,t}} \sigma_t \, dA, \quad N_{ak} = \int_{A_{ak}} \sigma_a \, dA, \quad N_{sj} = A_{sj}\sigma_{sj}, \quad N_p = A_p f_{ps}. \\ N_{cc} + N_{ct} + \sum_{k=u,w,l} N_{ak} + \sum_j N_{sj} + N_p = 0. \\ M_u = \int_{A_c} \sigma_c \, (y)(y-c)dA + \sum_{k=u,w,l} \int_{A_{ak}} \sigma_a \, (y)(y-c)dA + \sum_j N_{sj} \, (y_{sj} - c) + N_p(y_p - c). \end{cases} \tag{4}$$

In the UHPC moment integral, $\sigma_c(y)$ denotes the signed tensile or compressive concrete stress. The indices u, w, l identify the upper flange, web and lower flange. Solving axial equilibrium determines c; 0.1 mm layer integration then gives M_u. For an initial neutral-axis estimate, the compression resultant can be written $C_c = \alpha_c f_c bc$, so $c \simeq (T_{ct} + T_a + T_s + T_p - C_a - C_s)/(\alpha_c f_c b)$. The equivalent coefficient $\alpha_c = C_c/(f_c bc)$ is evaluated from the same net-area compression envelope; subsequent equilibrium iteration retains the actual flange and web geometry. To compare resistance on a common basis, the total peak load is converted using the 775 mm shear span: $M_{exp} = P_m(0.775)/2$. The five-beam comparison is given in Table 4.

Table 4. Comparison of experimental, FE and calculated ultimate moments

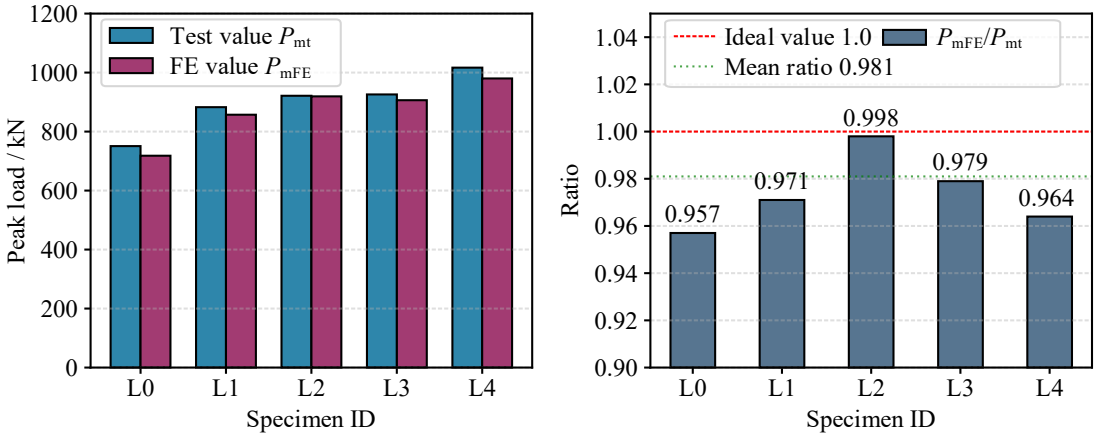
Beam	Mexp (kN·m)	MFE (kN·m)	Mcalc (kN·m)	Mcalc/Mexp	MFE/Mexp
L0	298.16	285.34	289.42	0.971	0.957
L1	348.06	337.97	340.85	0.979	0.971
L2	369.24	368.50	376.27	1.019	0.998
L3	368.22	360.49	383.62	1.042	0.979
L4	404.01	389.47	414.93	1.027	0.964
Mean	/	/	/	1.008	0.974
Sample SD	/	/	/	0.031	0.016

From Table 4, the calculated-to-test ratios range from 0.971 to 1.042, with a mean of 1.008 and a sample standard deviation of 0.031. The largest absolute difference is 4.2%. The FE-to-test mean is 0.974. The section formulation captures the resistance of the investigated beams while accounting for UHPC tensile resistance, embedded-steel forces and the prestressing stress increment.

3.4 Finite Element Parameter Expansion Analysis and Sensitivity Evaluation of Influencing Factors

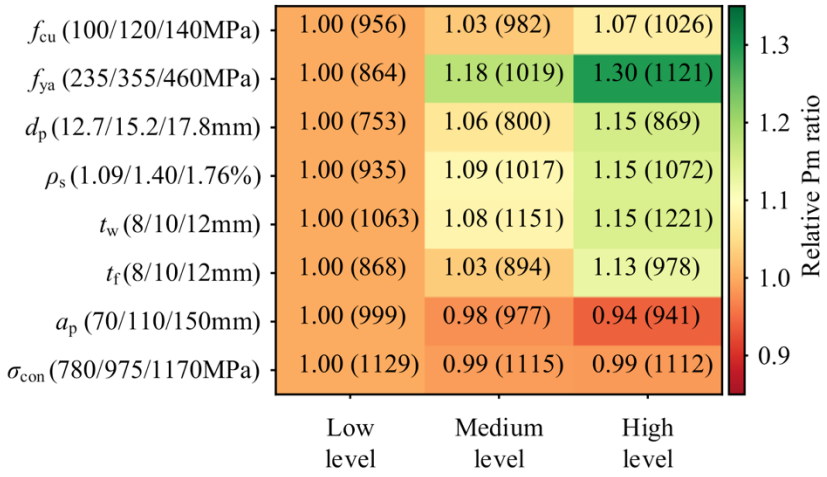
To make sure the correctness of the Finite Element Model (FEM), the peak load simulation values of 5 test beams were compared with the measured values. The outcomes are exhibited in Figure 8. In Figure 8, the FE-to-test peak-load ratios range from 0.957 to 0.998, with a mean of 0.974 and a sample standard deviation of 0.016. The FE results reproduce the relative resistance of the five beams. The parameter study contains 24 cases, arranged as eight three-level groups. Figure 9(a) compares their normalized peak loads; Figure 9(b) compares the measured average crack spacing with the estimates from JGJ 369-2016.

From Figure 9(a), based on the low level as the reference, the normalized ratios of peak loads at different levels of each parameter reflected the parameter sensitivity. The color scale range of the YS of SSs (fya, 235→460 MPa) was the largest, with the peak load increase ranging from +17.0% to +31.0%, implying that increasing the strength of SSs was the most effective way to enhance the BC. The increase in the diameter of prestressed reinforcement (dp, 12.7→17.8 mm) was +6.5% to +16.0%, and it also had a relatively obvious effect on the enhancement of the BC. The increase in the thickness of the web (tw, 8→12 mm) and the reinforcement ratio (ρs, 1.09%→1.76%) was +7.1% to +13.9% and +7.1% to +12.7% respectively, which were medium-sensitive parameters. The increase in the thickness of the flange (tf, 8→12 mm) was +4.1% to +11.8%. The increase in the CS of UHPC (fcu, 100→140 MPa) was +3.1% to +7.4%, which contributed to the peak load to some extent but with a limited amplitude.

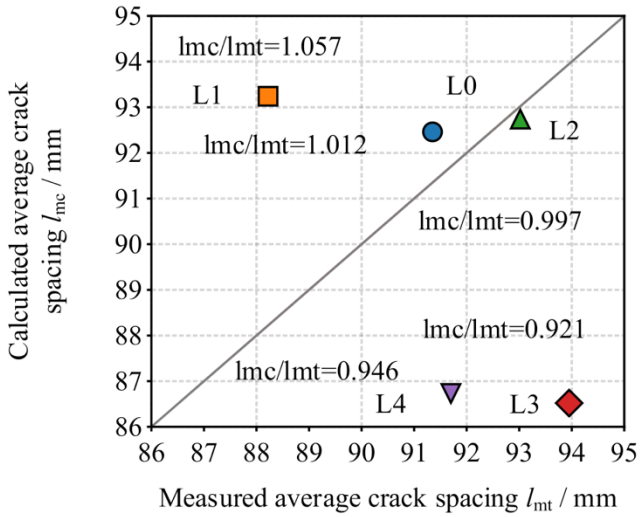


(a) Comparison of Test and FE Peak Capacity (b) FE/Test Bearing Capacity Ratio

Fig. 8. Comparison between the simulated peak load values and the actual measured values



(a) Normalized Heatmap of Peak Load in Parametric Analysis (Values are ratios to low level; parentheses show actual Pm/kN)

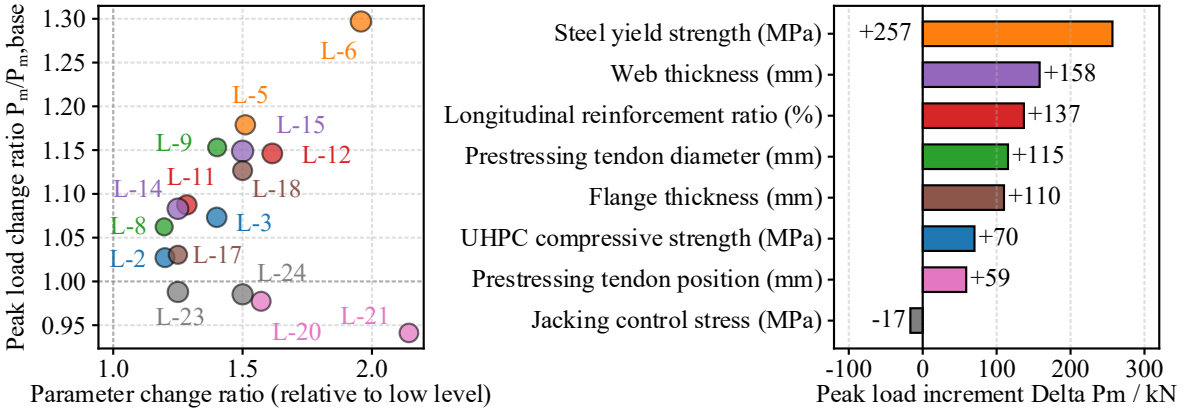


(b) Calculated vs. Measured Average Crack Spacing (mean=0.986, MSE=0.048, COV=0.049)

Fig. 9. Comparison between the heat map of parameter analysis outcomes and the crack spacing distribution

The position of the prestressed reinforcement (ap, 70→150 mm) was negatively correlated, with a peak load reduction of -3.6% to -7.0%, implying that the upward shift (increase in ap) of the prestressed reinforcement position would weaken the BC. The tension control stress (σcon, 780→1170 MPa) had almost no effect on the peak load (change rate -0.1% to +0.1%), and its main effect was to improve the CL. Comprehensive analysis showed that the YS of SSs and the configuration of prestressed reinforcement were the two dominant parameters affecting the peak load, followed by the thickness of the web and the reinforcement ratio. The CS of UHPC and the thickness of the flange had moderate influence. The tension control stress mainly affected the cracking performance and had an extremely low contribution to the UBC.

Figure 9(b) shows the comparison between the measured values of the average crack spacing of the five test beams and the calculated values of the JGJ 369-2016 reference. The data points are overall distributed near the diagonal. The mean ratio of the two is 0.986, the mean square error is 0.048, and the coefficient of variation is 0.049. Among them, L2 has the best agreement, with a ratio of 0.997, L3 is slightly lower, with a ratio of 0.921, and the ratios of the remaining specimens range from 0.921 to 0.997. The test beam in this article is not a pure UHPC component. The crack spacing is still controlled by macro parameters such as steel bar diameter, reinforcement ratio, protective layer thickness and prestress level. The JGJ 369-2016 formula can reflect these factors. At present, UHPC special standards such as NF P18-470 and T/CCES 01-2020 mainly stipulate material properties, tensile constitutive and design principles, and have not yet given a unified formula for the average crack spacing that directly corresponds to the components in this article. Therefore, this article uses JGJ 369-2016 as the comparative benchmark for prestressed concrete, but when using it for UHPC, fiber bridging, fiber orientation and tensile softening need to be considered. The relative and absolute peak-load changes for the 24 parameter cases are shown in Figure 10.



(a) Relative Sensitivity Bubble Chart

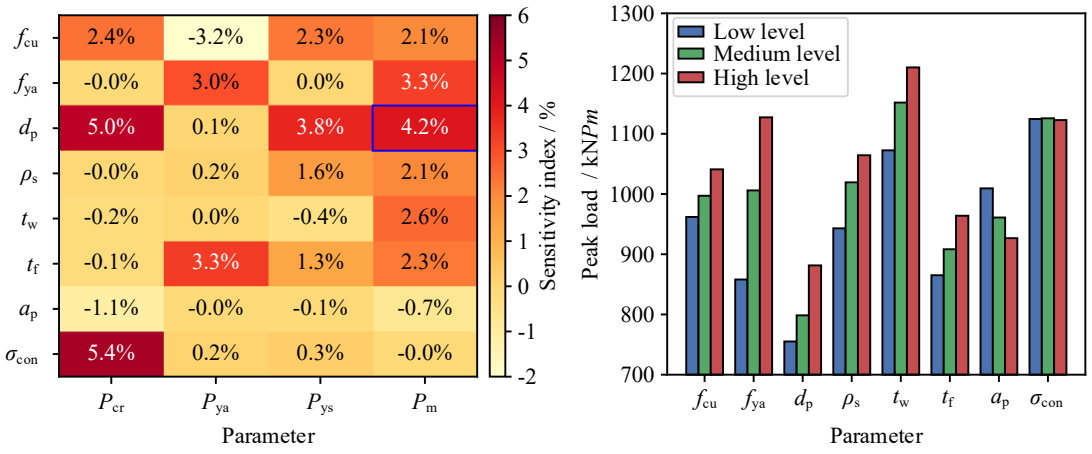
(b) Absolute Increment of Peak Load (High level minus low level)

Fig. 10. Sensitivity analysis of the impact of various design parameters on the peak load

Figure 10(a) is the sensitivity bubble plot. The horizontal axis represented the parameter variation rate (relative to the low level), and the vertical axis represented the peak load variation rate. The area of the bubbles was proportional to the absolute peak load. From the overall trend of the scatter plot distribution, the influence of the parameters on the peak load could be divided into three tiers. The first tier consisted of the YS of the SS (fya, orange bubble) and the diameter of the prestressing reinforcement (dp, green bubble): When the parameter variation rate of fya increased from 1.51 to 1.96, Pm/Pm,base jumped from 1.17 to 1.31. When the parameter variation rate of dp increased from 1.20 to 1.40, Pm/Pm,base rose from 1.07 to 1.16, and both had the highest relative sensitivity to the BC. The second tier included the thickness of the web (tw, purple bubble, up to 1.15), the reinforcement ratio (ρs, red bubble, up to 1.14), and the thickness of the flange (tf, brown bubble, up to 1.13), which had a moderate positive contribution to the BC. The third tier consisted of the CS of UHPC (fcu, blue bubble, Pm/Pm,base increased from 1.03 to 1.07) and the position of the prestressing reinforcement (ap, pink bubble). When the parameter variation rate of ap increased from 1.57 to 2.14, Pm/Pm,base dropped to 0.97 and 0.94 respectively, showing a negative correlation, that is, the upward movement of the prestressing reinforcement (increased ap) would

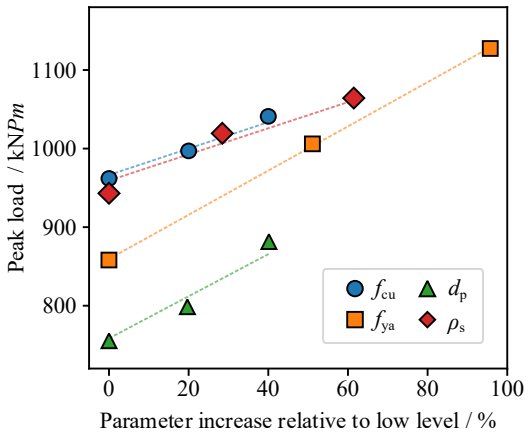
weaken the BC. Although the parameter variation rate of the tension control stress (σcon, gray bubble) increased from 1.25 to 1.50, Pm/Pm,base almost remained at 1.00, implying that σcon had almost no effect on the peak load within the range of 780–1170 MPa, and its main effect was to increase the CL.

From Figure 10(b), when the YS of the SS was optimized from a low level to a high level, the absolute increment of the peak load (ΔPm) was approximately +257 kN. The thickness of the WP (+158 kN), the reinforcement ratio (+137 kN), and the diameter of the Prestressing Steel (PS) bars (+115 kN) followed, and these four factors constituted the main contribution source to the increase in BC. In summary, the YS of the SS and the configuration of the PS bars were the two dominant parameters affecting the peak load. If the section size was already limited and the efficiency of parameter adjustment was pursued, the priority should be to increase the SS strength and the diameter of the PS bars. If the max improvement of the UBC was pursued, the combination effect of increasing the WP thickness and the SS strength was the best. Although the absolute increment of the CS of UHPC was limited, it significantly improved the CL, and it still had value in scenarios with strict crack control requirements. The tension control recommendation should aim to meet the CL as the control target, and there was no need to over-tension for the UBC. Based on the parameter analysis, the comprehensive assessment of the sensitivity of 8 key parameters was conducted, and the outcomes are exhibited in Figure 11. The dimensionless secant sensitivity is $S_{ij} = [(R_{i,H} - R_{i,L})/R_{i,L}]/[(p_{j,H} - p_{j,L})/p_{j,L}]$. Here, R_i is a load response, p_j a design parameter, and subscripts L and H denote low and high levels. The response percentage associated with a 10% parameter change is $100(0.10S_{ij}) = 10S_{ij}$ percent. Positive and negative values denote increasing and decreasing responses, respectively.



(a) Parameter Sensitivity Matrix Heatmap (Response change for a 10% parameter change)

(b) Peak Load Comparison by Parameter Group (Low/medium/high levels)



(c) Key Parameters vs. Peak Load

Fig. 11. Comprehensive sensitivity analysis of factors affecting load-BC

From Figure 11(a), the sensitivity index of the tension control stress σcon to the CL Pcr was the highest (5.4%), implying that the tension control stress was the key parameter for controlling the cracking performance. The sensitivity index of the pre-stressing bar diameter dp to the peak load Pm was the most prominent in the Pm column (4.2%), and the sensitivity indices to Pcr and Pys were 5.0% and 3.8% respectively, suggesting that the pre-stress strength had a positive contribution to both the BC and the cracking performance. The sensitivity index of the SP flange thickness tf to the SP yield load Pya was 3.3%, and to Pm was 2.3%. The sensitivity index of the SP of YS fya to Pm was 3.3%, and to Pya was 3.0%. The sensitivity index of the CS of UHPC fcu to Pm was 2.1%, and to Pcr was 2.4%. The sensitivity index of the SP web thickness tw to Pm was 2.6%. The tension control stress σcon had a relatively prominent influence on Pcr (sensitivity index 5.4%), but had almost no influence on Pm, implying that the tension control stress mainly contributed to the cracking stage. The implication of the pre-stressing bar position ap on all response indicators was negative, suggesting that the downward movement of the pre-stressing bar position (ap reduction) could increase the peak load.

In Figure 11(b), the high-value column of the SS YS group (fya) (1127.41 kN) increased by 31.38% compared to the low-value column (858.13 kN), with the most significant increase; the high-value column of the PS diameter group (dp) (881.59 kN) increased by 16.72% compared to the low-value column (755.28 kN), with the second largest increase. The peak load of the PS position group (ap) decreased with the increase of the position parameter (i.e., the upward movement of the PS position), and the high-value column (926.81 kN) decreased by 8.19% compared to the low-value column (1009.48 kN); the column height of the tension control stress group (σcon) changed very little (1124.71 – 1122.79 kN), implying that this parameter had a limited influence on the peak load. Figure 11(c) further analyzed the corresponding relationship between the values of the four key parameters (fcu, fya, dp, ρs) and the peak load Pm. The dotted line was the linear fitting trend line. From the slope of the trend lines of each parameter, the slope of the PS diameter dp was the largest (3.15 kN/%), implying that the marginal improvement of the unit relative increase had the highest impact on Pm. The SS YS fya was second (2.81 kN/%). The LR ratio ρs was 1.96 kN/%. The CS of UHPC was the smallest (1.98 kN/%). Comprehensive analysis of the three panels showed that the influence of the SS YS on the peak load was the most significant, followed by the prestressing force, reinforcement ratio, and the thickness of the steel web. The influence of the CS of UHPC was relatively limited. The tension control stress mainly affected the CL, and its influence on the peak load could be ignored. It was recommended that in engineering design, the type of steel and the prestressing configuration should be optimized first, and the matching of the reinforcement ratio and the thickness of the steel web should also be considered.

4. Conclusions

This study examined the flexural behavior and ultimate moment capacity of prestressed steel-UHPC composite beams through five beam tests, OpenSees analysis and a section equilibrium formulation. The combined investigation clarifies how prestressing strands and embedded steel sections influence cracking resistance, load capacity and deformation, providing a basis for selecting parameters according to different structural performance requirements. The proposed formulation incorporates UHPC compression and fiber tension, the forces in the upper flange, web and lower flange of the steel section, longitudinal reinforcement and prestressing strands. Plane-section compatibility links these components, while axial force and moment equilibrium determine the sectional resistance. The calculated-to-test moment ratios range from 0.971 to 1.042, with a mean of 1.008 and a sample standard deviation of 0.031. The maximum absolute difference is 4.2%. For the investigated sections, a compressive strength coefficient of 0.85 relative to cube strength and a limiting compression strain of 0.0035 are adopted. The equivalent compression block provides an initial neutral-axis estimate that can be refined through axial equilibrium.

The parametric results distinguish the factors governing cracking from those governing peak resistance. Increasing steel yield strength from 235 to 460 MPa increases peak load by 31.38%, whereas increasing strand diameter from 12.7 to 17.8 mm produces a 16.72% increase. Strand diameter exhibits the greatest normalized sensitivity of peak load, while jacking stress primarily improves cracking resistance. These differences indicate that the largest gain over a specified

parameter range does not necessarily correspond to the highest normalized sensitivity. Prestressing increases the cracking load of L2 by 68.3% relative to L0. However, deflection ductility ranges from 1.76 to 2.66 and does not increase uniformly with prestress, indicating that resistance enhancement must be considered together with deformation demand. Parameter selection should therefore balance prestressing degree, steel-section ratio and strand configuration to satisfy cracking, capacity and ductility requirements. The identified trends and section formulation apply to the investigated geometries, reinforcement arrangements and monotonic loading conditions.

Acknowledgement

The research is supported by: Yangzhou Construction Science and Technology Project "Research on Flexural Performance and Design Method of Prestressed Steel-Reinforced RPC Beams", Project No.: 202302.

References

[1] Fang Z, Tian X, Peng F. Flexural strength of prestressed Ultra-High-Performance concrete beams. Engineering Structures. 2023;279:115612. https://doi.org/10.1016/j.engstruct.2023.115612
[2] Zhang Y, Wang H, Qin Y, Huang S, Fan W. Experimental and analytical studies on the flexural behavior of steel plate-UHPC composite strengthened RC beams. Engineering Structures. 2023;283:115834. https://doi.org/10.1016/j.engstruct.2023.115834
[3] Xu B, Liu Y, Zhu W. Comparative study on flexural behavior of steel-UHPC composite beams and steel-ordinary concrete composite beams in the negative moment zone. Structures. 2023;57:105288. https://doi.org/10.1016/j.istruc.2023.105288
[4] Ahmed Ibrahim O. Enhancing Composite Steel-Concrete Beams: A Review of Strengthening Techniques, Performance, and Practical Applications. ERU Research Journal. 2025;4(4):3336-3356. https://doi.org/10.21608/erurj.2025.366922.1234
[5] Williams M, Menon D, Prasad AM. Creep and Shrinkage in Prestressed Concrete Beams: An Experimental Study. Structural Concrete. 2024;25(4):2400-2419. https://doi.org/10.1002/suco.202300625
[6] Kim YJ, Gebrehiwot H. Shear Capacity of Glass Fiber-Reinforced Polymer-Reinforced Ultra-High-Performance Concrete Beams without Stirrups. ACI Structural Journal. 2023;120(2):47-59. https://doi.org/10.14359/51734823
[7] Abadel AA, Baktheer A, Emara M, Ghallah M, Hamoda A. Flexural behavior of precast concrete-filled steel tubes connected with high-performance concrete joints. Materials Science-Poland. 2024;42(3):72-85. https://doi.org/10.2478/msp-2024-0032
[8] El-Bosiely M, Nabil A, Meleka NN, Eltaly B. Enhancing the Behavior of Concrete Beams Reinforced with FRP Bars Using Embedded Steel Sections and Ultra-high-performance Strain-Hardening Cementitious Composite. International Journal of Civil Engineering. 2025;23(6):1115-1135. https://doi.org/10.1007/s40999-025-01084-2
[9] Zhang JH, He J, Tan C, Feng SD, Wang ZT. Parametric Analysis of Composite Slab with Steel Bar Trusses at Construction Stages. Journal of China & Foreign Highway. 2025;45(1):235-243. https://doi.org/10.14048/j.issn.1671-2579.2025.01.029
[10] Jamadin A, Kudus SA, Ya'akob ADH, Misnan MF, Jaini ZM. Vibration-Based Finite Element Model Analysis on Dynamic Characteristics of Ultra-High Performance Concrete Beam. International Journal of Integrated Engineering. 2023;15(7):213-223. doi: https://doi.org/10.30880/ijie.2023.15.07.020
[11] Shwalia ASI, Al-Salim NHA. Investigating the influence of UHPC layer length on the flexural response of prestressed concrete I-beams. Advances in Bridge Engineering. 2025;6(1):36. https://doi.org/10.1186/s43251-025-00183-3
[12] Lai ZC, Yao PY, Yang XQ, Li SH, Zhao Q. Flexural behavior and design of high-strength I-shaped steel-UHPC composite beams. Advances in Structural Engineering. 2025;28(10):1877-1889. https://doi.org/10.1177/13694332251319094
[13] Galano S, Losanno D, Miluccio G, Parisi F. Multidimensional Nonlinear Numerical Simulation of Post-tensioned Concrete Girders with Different Prestressing Levels. Structural Concrete. 2023;24(6):7021-7042. https://doi.org/10.1002/suco.202300272
[14] Huang Z, Lin G, Huang X, Li W, Sui L. Bond-slip constitutive model and numerical simulation of shaped steel embedded in UHPC. Industrial Construction. 2024;54(3):143-152. https://doi.org/10.13204/j.gyjzG21092803
[15] Sokoli D, Limantono A, To DV, Moehle JP, Ghannoum WM. From Global to Local Deformations of Concrete Frame Members Accounting for Steel Properties. ACI Structural Journal. 2025;122(3):133-145. https://doi.org/10.14359/51744380

[16] Franceschini L, Belletti B, Tondolo F, Sanchez Montero J. A Simplified Stress-Strain Relationship for the Mechanical Behavior of Corroded Prestressing Strands: The SCPS-model. Structural Concrete. 2023;24(1):189-210. https://doi.org/10.1002/suco.202200170
[17] Li B. Multi-scale Finite Element Analysis and Experimental Study on Cable-stayed Bridge with Steel-UHPC Composite Beams. Journal of Highway and Transportation Research and Development. 2023;40(11):131-141. https://doi.org/10.3969/j.issn.1002-0268.2023.11.015
[18] Nakari T, Tulonen J, Laaksonen A. Experimental study of stress increase of unbonded tendons in continuous post-tensioned concrete beams. Structural Concrete. 2025;26(4):4567-4582. https://doi.org/10.1002/suco.202401222
[19] Diab A, Ferche A. Modeling the response of UHPC shear-critical beams: Integrating nonlinear finite element analysis and artificial neural network. Structural Concrete. 2026;27(2):1364-1382. https://doi.org/10.1002/suco.70191